This manuscript is published in

IEEE Transactions on Circuits and Systems I: Regular Papers

Reference:

D. Widmann, M. Grözing, and M. Berroth, "Digital Time-Domain Predistortion of Linear Periodically Time-Varying Effects and Its Application to a 100-GS/s Time-Interleaved CMOS DAC," IEEE Transactions on Circuits and Systems I: Regular Papers, vol. 70, no. 12, pp. 5098-5109, 2023.

DOI: 10.1109/TCSI.2023.3311353

Digital Time-Domain Predistortion of Linear Periodically Time-Varying Effects and its Application to a 100-GS/s Time-Interleaved CMOS DAC

Daniel Widmann, Markus Grözing, *Member, IEEE*, and Manfred Berroth, *Senior Member, IEEE*

***Abstract*—In high-speed data transmission systems, CMOS digital-to-analog converters (DACs) at very high sampling rates are essential components allowing predistortion of the transmitted signal. Next to compensation of bandwidth limitations of the DAC and assembly, predistortion is also able to compensate other effects originating from time interleaving or from artifacts of the DAC circuit concept. Especially, linear, periodically time-varying (LPTV) effects are one source of impairments in the output signal causing spurious components and their compensation is of particular importance for time-interleaved systems. In this work, a universal predistortion concept including system identification based on the system's reactions to unit impulses at all corresponding positions in a period is presented and applied to a 28-nm CMOS DAC with time interleaving by an analog multiplexer at sampling rates up to 100 GS/s. Measurements of this DAC reveal LPTV effects with a period of 32 affecting the analog output signal that may be attributed to time interleaving as well as architecture. A theoretical problem description is given and sources of LPTV distortions are identified. Starting from the theoretical description, a universal N:1 predistortion method in time domain is deduced based on a simple system identification method. Measurements of single-tone signals reveal a signal-to-noise and distortion ratio improvement up to 13.5 dB and around 7 dB for a broadband, two-level pulse-amplitude modulated signal at 100 GS/s compared to a linear, time-invariant filter. The proposed predistortion concept is a universal method to compensate for any N:1 LPTV artifacts with significant reduction of LPTV distortions and can be translated to a common transversal filter structure.**

***Index Terms*—Analog-digital integrated circuits, arbitrary waveform generator, CMOS integrated circuits, digital-analog conversion, digital-to-analog converter, digital filters, mixed-signal integrated circuits, predistortion, pulse-amplitude modulation, signal processing algorithms, time-varying channels, time-varying systems, transmitters.**

I. Introduction

HIGH-SPEED digital-to-analog converters (DACs) are key components in electrical as well as in optical transmission systems [1]–[6]. Predistortion in digital domain is fundamental to compensate for the transfer function including bandwidth limitations and finally, to reduce intersymbol interference (ISI). However, simple linear, time-invariant (LTI) approaches may be insufficient to compensate for all effects of DAC realizations. Especially, time-interleaved systems, e.g. systems using an analog multiplexer (AMUX) [7], may require a multiple-input and multiple-output (MIMO) or multiple-input and single-output (MISO) description and predistortion, respectively. Other sources of distortions can be caused by periodic effects due to conceptual reasons. A powerful frequency-domain predistortion of a 2:1 system is presented in [8]–[10] which may be extended to N:1.

In this work, a universal time-domain predistortion method including system identification for linear, periodically time-varying (LPTV) N:1 systems is presented and applied to a time-interleaved DAC in 28-nm fully-depleted silicon-on-insulator (FD-SOI) CMOS technology for sampling rates up to $f_\mathrm{s} = 100\,\mathrm{GS/s}$. The interleaving depth is 2:1 and in combination with internal LPTV effects, a 32:1 LPTV system has to be considered in total. LPTV artifacts can have massive influence on performance in terms of deteriorated signal quality. To compensate for these impairments, an appropriate LPTV predistortion concept is required as an LTI predistortion approach is insufficient. The predistortion method is evaluated by single-tone measurements revealing a signal-to-noise and distortion ratio ($SNDR$) improvement of up to $13.5\,\mathrm{dB}$ as well as by broadband pulse-amplitude modulated (PAM) signals. In the case of PAM signals, the results are compared to predistortion based on a training sequence.

The article is organized as follows. In Section II, definitions and notations are given for theoretical descriptions required for this work. Next, the origin of distortions due to deterministic LPTV effects is derived in Section III based on a model of nonuniform holding signals with variations in sampling periods and gain variations. In Sections IV and V, the investigated system is presented and sources of LPTV effects in the given CMOS DAC are identified coinciding with an LPTV period of $P = 32$. Different system identification methods and predistortion techniques are given in Section VI with the universal LPTV predistortion concept in Section VI-C. Finally, measurement results are presented in Section VII divided into the estimation of the impulse response and measurements of single-tone as well as broadband PAM signals followed by the conclusion.

II. Definitions and Notations

Throughout this work, the following definitions and notations are used. The continuous-time impulse response $h(t, \tau)$ is defined as the response of a linear system with system operator

This project is funded by the *Deutsche Forschungsgemeinschaft* (DFG, German Research Foundation) — 276016065.

Daniel Widmann, Markus Grözing, and Manfred Berroth are with the Institute of Electrical and Optical Communications Engineering, University of Stuttgart, 70569 Stuttgart, Germany (e-mail: daniel.widmann@int.uni-stuttgart.de).

$\mathcal{T}$ at observation instant t to an input Dirac impulse $\delta(t-\tau)$ at instant of time τ [11]:

$$h(t,\tau) \coloneqq \mathcal{T}\{\delta(t-\tau)\} \ . \tag{1}$$

Generally, a two-dimensional impulse response being a function of the two independent variables t and τ has to be considered. For LTI systems, it holds $h(t,\tau) = h(t-\tau)$. The output signal $y\,(t)$ of a linear system with input $x\,(t)$ can be expressed as a superposition integral

$$y(t) = \int_{-\infty}^{\infty} x\,(\tau)\,h\,(t,\tau)\,\mathrm{d}\tau =: x\,(t) \circledast h\,(t,\tau) \tag{2}$$

where $\circledast$ denotes the time-variant convolution. In this work, the modified, time-variant impulse response or (input) delay-spread function [11], [12] $g\,(t,\gamma)$ is of special importance. A transformation of variables according to

$$\tau = t - \gamma \tag{3}$$

results in

$$g\,(t,\gamma) \coloneqq h\,(t,t-\gamma) \ . \tag{4}$$

It can be interpreted as the response of the system at observation time instant t to an input Dirac impulse being active at time $t-\gamma$, i.e. at a time step γ earlier [11]. Therefore, (2) can be rewritten as

$$\begin{aligned} y(t) &= \int_{-\infty}^{\infty} x\,(t-\gamma)\,h\,(t,t-\gamma)\,\mathrm{d}\gamma = \int_{-\infty}^{\infty} x\,(t-\gamma)\,g\,(t,\gamma)\,\mathrm{d}\gamma \\ &\overset{\zeta=t-\gamma}{=} \int_{-\infty}^{\infty} x\,(\zeta)\,g\,(t,t-\zeta)\,\mathrm{d}\zeta =: x(t) \circledast g\,(t,\gamma) \ . \end{aligned} \tag{5}$$

Moreover, another definition of an impulse response $\tilde{h}\,(\rho,\tau)$ is useful in system identification which is normalized in time by

$$\rho \coloneqq t - \tau \tag{6}$$

yielding

$$\tilde{h}\,(\rho,\tau) \coloneqq h\,(\rho+\tau,\tau) \ , \tag{7}$$

i.e., it describes the response to a Dirac impulse at time τ at a time step ρ later.

The class of LPTV systems [13]–[16] is of special importance for this work. More precisely, deterministic LPTV systems are considered. For these systems with normalized period $P \in \mathbb{N}$, it holds

$$h\,(t + P\cdot T_\mathrm{s}, \tau + P\cdot T_\mathrm{s}) = h\,(t,\tau) \tag{8}$$

as well as

$$g\,(t + P\cdot T_\mathrm{s}, \gamma) = g\,(t,\gamma) \tag{9}$$

and

$$\tilde{h}\,(\rho, \tau + P\cdot T_\mathrm{s}) = \tilde{h}\,(\rho,\tau) \ , \tag{10}$$

respectively. $T_\mathrm{s} = 1/f_\mathrm{s}$ denotes the sampling period.

Analogously, discrete-time representations can be defined. With

$$\delta\,[n] = \begin{cases} 1 & \text{for } n = 0 \ , \\ 0 & \text{for } n \neq 0 \end{cases} \tag{11}$$

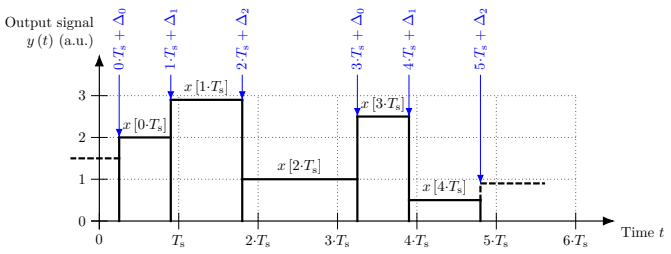

Fig. 1. Periodic, nonuniform holding signal with period $P = 3$ [16], [19], [20].

it holds

$$h\,[n,\nu] \coloneqq \mathcal{T}\{\delta\,[n-\nu]\} \ , \tag{12}$$

$$y\,[n] = \sum_{\nu=-\infty}^{\infty} x\,[\nu]\,h\,[n,\nu] \tag{13}$$

as well as

$$\begin{aligned} y\,[n] = x\,[n] \circledast g\,[n,\nu] &= \sum_{\nu=-\infty}^{\infty} x\,[\nu]\,g\,[n,n-\nu] \\ &= \sum_{\nu=-\infty}^{\infty} x\,[n-\nu]\,g\,[n,\nu] \ . \end{aligned} \tag{14}$$

Equations (8) to (10) hold equivalently for the discrete-time representations.

III. Problem Statement

A theoretical description of LPTV behavior of DACs is given in this section. The observed behavior can be described by a combination of deterministic, periodic jitter as well as periodic gain variations. For simplification, the theoretical description is divided into the linear description of periodically nonuniform holding times and periodic variations of gain. For comparison, the output $Y_\mathrm{ZOH}\,(\mathrm{j}\omega)$ of a DAC with ideal zero-order hold (ZOH) operation without quantization in frequency domain is given in (15) with the angular frequency ω, $\mathrm{si}\,(x) \coloneqq \sin\,(x)\,/x$ and the spectrum $X\,(\mathrm{j}\omega)$ of an analog input signal $x\,(t)$ before sampling.

$$Y_\mathrm{ZOH}\,(\mathrm{j}\omega) = \left[\sum_{\nu=-\infty}^{\infty} X\left(\mathrm{j}\omega + \mathrm{j}\nu\frac{2\pi}{T_\mathrm{s}}\right)\right] \cdot \mathrm{si}\left(\frac{\omega T_\mathrm{s}}{2}\right) \mathrm{e}^{\,-\,\mathrm{j}\omega T_\mathrm{s}/2} \tag{15}$$

Replicas of $X\,(\mathrm{j}\omega)$ shifted by $\nu\cdot 2\pi/T_\mathrm{s}$ related to the sampling period T_s and a $\sin\,(x)\,/x$ roll-off are typical characteristics.

Impacts of nonuniform holding times on the output spectra of DACs are well-known and often considered in terms of timing mismatch or jitter, respectively [17]–[20]. In the following, a DAC output signal with periodic, nonuniform ZOH behavior which is illustrated in Fig. 1 is considered. A more detailed derivation is given in the appendix. To show these effects analytically, the result of the model according to [17]–[20] shall be given in this paragraph assuming a jittered clock. Let P define the period normalized to the sampling period T_s.

The output spectrum for a DAC output signal with periodic, nonuniform ZOH behavior can be described by [19], [20]

$$Y(\mathrm{j}\omega) = \frac{1}{PT_\mathrm{s}} \sum_{\nu=-\infty}^{\infty} A_\nu(\mathrm{j}\omega)\, X\left(\mathrm{j}\omega - \mathrm{j}\nu\frac{2\pi}{PT_\mathrm{s}}\right) . \quad (16)$$

The terms $A_\nu(\mathrm{j}\omega)$ are given in the appendix. In case of the absence of jitter ($P = 1$, $\Delta_p = 0$), (16) and (50b) result in the well-known ZOH behavior given in (15) with a $\sin(x)/x$ roll-off. Apart from the terms $A_\nu(\mathrm{j}\omega)$ and the scaling factor, an essential difference to ideal ZOH behavior described in (15) is the observation that $X(\mathrm{j}\omega)$ is replicated at intervals of $2\pi/(PT_\mathrm{s})$ which is reduced by a factor of $1/P$. Thus, more distortions ($\nu \neq 0$) are expected.

Similarly, the effect of periodic gain variations yields in such kind of distortions and is described separately. So far, the model considered the influence of pure, periodic clock jitter. A description of pure, periodic gain variations can be described as follows. Assuming an input signal $x(t)$ suffering from linear gain variations $\epsilon_\mathrm{G}(t)$, the resulting signal $y(t)$ can be expressed as

$$y(t) = x(t)\,(1 + \epsilon_\mathrm{G}(t)) . \quad (17)$$

Taking the Fourier transform of (17) yields

$$Y(\mathrm{j}\omega) = X(\mathrm{j}\omega) + \frac{1}{2\pi} X(\mathrm{j}\omega) * \varepsilon_\mathrm{G}(\mathrm{j}\omega) \quad (18)$$

where $*$ denotes the convolution. Considering P periodic variations, (17) can be rewritten using a Fourier series with coefficients $c_{\epsilon_\mathrm{G},\nu}$ in time domain as

$$y(t) = x(t)\left(1 + \sum_{\nu=-\infty}^{\infty} c_{\epsilon_\mathrm{G},\nu}\, \mathrm{e}^{\mathrm{j}\nu\frac{2\pi}{PT_\mathrm{s}}t}\right) . \quad (19)$$

and in frequency domain as

$$Y(\mathrm{j}\omega) = X(\mathrm{j}\omega) + \sum_{\nu=-\infty}^{\infty} c_{\epsilon_\mathrm{G},\nu} \cdot X\left(\mathrm{j}\omega - \mathrm{j}\nu\frac{2\pi}{PT_\mathrm{s}}\right) . \quad (20)$$

This result reveals similar distortions as in (16) due to spectral replicas at intervals of $2\pi/(PT_\mathrm{s})$.

The aim of the predistortion concept will be the cancellation or reduction of these spurs caused by LPTV behavior.

IV. System Overview and Circuit Implementation

The system realized in 28-nm FD-SOI CMOS technology consists of two sub-DACs with a nominal resolution of 8 bit and an AMUX at their outputs performing 2:1 time interleaving in the analog domain and doubling the sampling rate. It is presented in [21]. Fig. 2 illustrates the system. An additional on-chip 256 KiByte = 256 KiS SRAM memory completes the system to an arbitrary waveform generator (AWG). Both the sub-DACs as well as the AMUX operate at half-rate clocks: the sub-DACs' output circuits are clocked at $f_\mathrm{clk} = f_\mathrm{s}/4$, the AMUX at $f_\mathrm{clk} = f_\mathrm{s}/2$. Concerning circuit topology, the sub-DACs are realized in CMOS topology whereas the AMUX as well as the respective clock path are realized in current-mode topology. The 8-bit sub-DACs are implemented in a pseudo-segmented structure [22], [23]. I.e., the four least significant bits

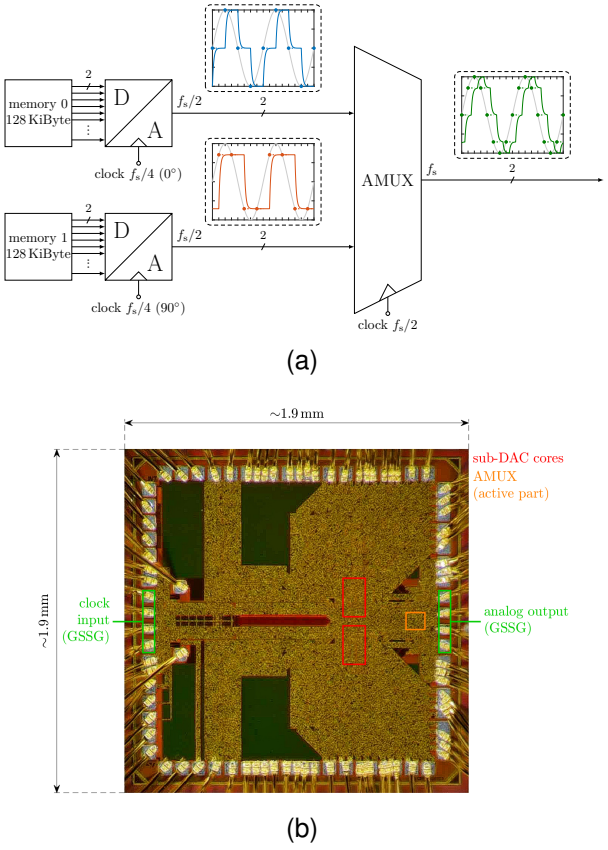

Fig. 2. (a) System overview. (b) Chip micrograph. Next to sub-DACs and AMUX, on-chip memory, clock path as well as supply voltage decoupling capacitances are implemented.

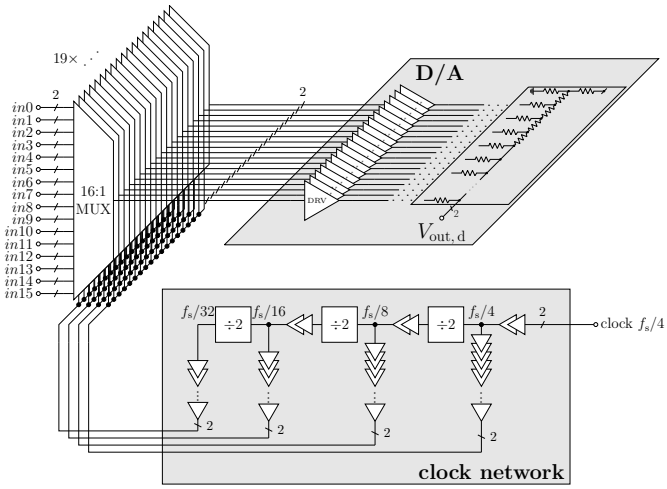

Fig. 3. Block diagram of one sub-DAC core [21].

are realized in an R-$2R$ part with inherent binary weighting and the four most significant bits are represented by 15 unary paths like a thermometer DAC. In contrast to a real themometer DAC, a passive binary-weighting decoder instead of a thermometer decoder is used. Hence, 19 data channels represent the digital 8-bit word of each sub-DAC in total.

In Fig. 3, one of the sub-DAC cores is shown in more detail. It consists of a clock network, a serializer as well as the digital-

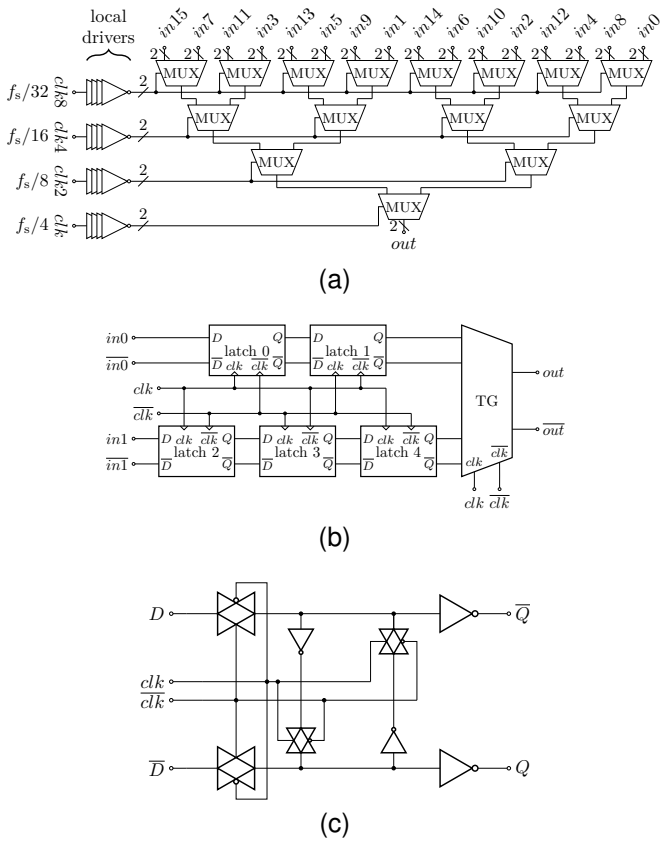

Fig. 4. (a) MUX tree for 16:1 serialization [21] and (b) single MUX stage [21], [24] where sampling is performed. MUX operation is realized by transmission gates (TG). Additional input inverters at each MUX stage are not drawn in (b). Local drivers at each MUX tree reduce the load of the global clock network in Fig. 3. In (c), the implementation of the CMOS latches is depicted.

to-analog output stage (D/A). The latter is realized by output drivers (DRV) and a resistor network providing a differential, analog output signal $V_{\mathrm{out,\,d}}$. Each differential serializer consists of 19 16:1 multiplexers (MUX) in a tree structure providing the data at $f_\mathrm{s}/2$ to the sub-DAC output drivers prior to the digital-to-analog conversion stage and is shown in Fig. 4a. A half-rate concept is applied in all MUX stages. The MUXs are realized in CMOS logic according to Fig. 4b and also perform data sampling. With every new branch, the MUX stages are scaled by a factor of two ensuring a constant load to all clock domains of the global clock network. In Fig. 4c, the latch topology is depicted. Supply voltage is separated into data and clock paths with individual decoupling capacitors. To drive the 19-channel serializer exhibiting a large load, a clock network with huge driving capability is required. Delay compensation as well as enhancement of driver capability requires long driver chains in the clock network in Fig. 3.

Finally, Fig. 5 shows the schematic of the current-mode AMUX with shunt and series peaking techniques for bandwidth enhancement.

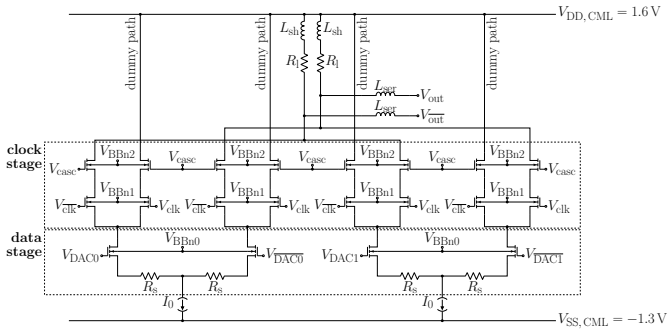

Fig. 5. Schematic of the AMUX [21].

V. Sources of LPTV Effects in the DAC Architecture

Considering the system overview in Fig. 2a, an obvious source of periodic deviations is given by the 2:1 interleaving due to the AMUX. As the clock drivers in the sub-DACs clock networks are realized as CMOS inverters, a high, dynamic load to the supply voltage with periodic repetitions is caused. The last data sampling is performed in the MUX stages at $f_\mathrm{s}/4$ according to Fig. 4b. Consequently, voltage deviations in the clock network have direct impact on the output samples of the MUX and hence on the analog DAC output. The sampled digital data is affected by variations in the clock signal which can lead to deviations in the sampling period as well as in the magnitude. However, due to the architecture of the sub-DAC clock network, the dynamic loading of the supply voltage is periodic with a period of 16 $f_\mathrm{s}/4$ half-clocks. The sub-DAC clock network's state repeats after eight $f_\mathrm{s}/4$ clock cycles or 16 sub-DAC output samples due to the half-rate clock architecture, respectively. In measurements, a periodic behavior with a period of $P = 32$ $f_\mathrm{s}/2$ half-clocks can be found. The observed period of $P = 32$ coincides with the periodicity in the sub-DACs' clock networks in combination with the 2:1 AMUX interleaving which is why the influence of the clock network on the output samples may be regarded as the source of LPTV distortions in the overall output signal. Hence, the system could be regarded as highly interleaved system. The effects of periodic supply voltage artifacts can be reduced by more on-chip decoupling capacitance but is limited by chip area restrictions. On the contrary, the current-mode AMUX driven by a current-mode clock path provides a constant load to the supply voltage which is why comparable LPTV distortions due to supply voltage instabilities is not expected for topological reasons. However, AMUX asymmetries can also cause LPTV effects.

To summarize, the sub-DAC architecture causing periodic supply voltage distortions affecting output sampling in the sub-DACs' serializers in combination with the AMUX time interleaving correlates with the experimentally determined period and suggests being a source for LPTV distortions in this DAC.

VI. System Identification and Predistortion Methods

For predistortion, adequate system identification is required. In a first approach, the system is characterized by the response to a training sequence. The results of the corresponding predistortion serve as reference for broadband PAM signals. However, this approach is an LTI method and it is therefore not suitable for a universal LPTV predistortion. Next, another well-known LTI predistortion method based on system identification using a single unit impulse is discussed. It serves as an intermediate step to develop the universal LPTV predistortion which is the core of this work.

A. LTI Predistortion Based on System Identification by a Training Sequence

For broadband PAM signals, an inverse filter can be determined by measuring the output $y\,[n]$ to a training input sequence $x\,[n],\ n \in \{0,\ldots,N-1\}$. Denoting the discrete Fourier transforms (DFTs) of $x\,[n]$ and $y\,[n]$ as $X\,[k]$ and $Y\,[k]$, $k \in \{0,\ldots,N-1\}$, the channel transfer function $H\,[k]$ can be determined by

$$H\,[k] = \frac{Y\,[k]}{X\,[k]}\ . \tag{21}$$

For a zero-forcing filter, the transfer function $E\,[k]$ of an inverse filter is given by [25]

$$E\,[k] = \frac{1}{H\,[k]}\ . \tag{22}$$

Alternatively, a minimum mean square error approach can be used considering noise in addition to the ISI. Throughout this work, proper normalization of data is assumed which is not depicted for simplification. Predistortion according to (22) with the same data sequence for training as well as for predistortion will be used as reference for broadband signals to evaluate the proposed method in this work. However, this LTI approach is not a universal predistortion method for compensation of LPTV effects of arbitrary signals. It only compensates effects properly for the dedicated broadband data sequence that is chosen for training.

B. LTI Predistortion Based on System Identification by a Single Unit Impulse

Considering the convolution of an LTI channel impulse response $h\,[n]$ of length N_h sampled at $t_0 + nT_\mathrm{s}$ ($n \in \{0,\ldots,N_\mathrm{h}-1\}$) and the one of a predistortion filter $e\,[n]$ of length N_e in time domain

$$e\,[n] * h\,[n] = \sum_{\nu=-\infty}^{\infty} e\,[\nu]\,h\,[n-\nu] = \sum_{\nu=0}^{N_\mathrm{e}-1} e\,[\nu]\,h\,[n-\nu]\ , \tag{23}$$

a Nyquist impulse $\delta\,[n-n_0]$ at position n_0 is sought. Thus, the condition to comply with the first Nyquist criterion can be written as in (24) with the help of a convolution matrix $\boldsymbol{H}$ of size $(N_\mathrm{e}+N_\mathrm{h}-1)\times N_e$, the vector $\boldsymbol{e}$ of size $N_\mathrm{e}\times 1$ with predistortion filter coefficients, the Nyquist impulse vector $\boldsymbol{i}$ and an error vector $\boldsymbol{\epsilon}_\mathrm{i}$ both of size $(N_\mathrm{e}+N_\mathrm{h}-1)\times 1$ [26]. The position of the marked element $h\,[0]$ depends on the size of the matrix. Minimizing the energy of the error, a least squares (LS) solution $\boldsymbol{e}_\mathrm{LS}$ is given using the pseudoinverse

$$\boldsymbol{H}^{+} = \left(\boldsymbol{H}^\mathrm{H}\boldsymbol{H}\right)^{-1}\boldsymbol{H}^\mathrm{H} \tag{25}$$

yielding

$$\boldsymbol{e}_\mathrm{LS} = \left(\boldsymbol{H}^\mathrm{H}\boldsymbol{H}\right)^{-1}\boldsymbol{H}^\mathrm{H}\boldsymbol{i} = \boldsymbol{H}^{+}\boldsymbol{i}\ . \tag{26}$$

The operator $(\cdot)^\mathrm{H}$ denotes the conjugate transpose of the matrix. Again, a zero-forcing solution is considered. This LTI method will be insufficient and is not able to compensate for LPTV artifacts. However, it is the starting point for an LPTV predistortion.

C. LPTV Predistortion Based on System Identification by Shifted Unit Impulses

Inspired by the method in section VI-B, a universal extension for LPTV systems is derived. Defining

$$h\,[n,\nu] = h\,(t_0 + nT_\mathrm{s}, t_0 + \nu T_\mathrm{s}) \tag{27}$$

and considering

$$\begin{aligned}\sum_{\nu=n-N_\mathrm{h}+1}^{n} e\,[\nu]\,h\,[n,\nu] &= \sum_{\nu=n-N_\mathrm{h}+1}^{n} e\,[\nu]\,\tilde{h}\,[n-\nu,\nu] \\ &\overset{\mu=n-\nu}{=} \sum_{\mu=0}^{N_\mathrm{h}-1} e\,[n-\mu]\,\tilde{h}\,[\mu,n-\mu]\ ,\end{aligned} \tag{28}$$

an appropriate convolution matrix for the LPTV case is found in (29) with a size of $(N_\mathrm{e}+N_\mathrm{h}-1)\times N_\mathrm{e}$. Again, the position of the marked element $\tilde{h}\,[0,P-1]$ depends on the size of the matrix. In (28), finite length as well as causality are considered in the bounds of summation. The convolution matrix is described by

$$\boldsymbol{H}_\mathrm{LPTV} = \left(\hat{\boldsymbol{h}}_0, \hat{\boldsymbol{h}}_1, \ldots, \hat{\boldsymbol{h}}_{N_\mathrm{e}-1}\right) \tag{30}$$

where the column vectors $\hat{\boldsymbol{h}}_i$ contain the impulse reactions $\tilde{h}\,[\mu,(n-\mu)\bmod P]$ complemented by zero padding and subjected to an appropriate shift. Moreover, N_e is chosen to be a multiple of P. According to (24), Nyquist impulse vectors $\boldsymbol{i}_\kappa \in \mathbb{R}^{N_\mathrm{e}\times 1}$, $\kappa \in \{0,\ldots,P-1\}$ have to be defined for Nyquist impulses at different positions. In contrast to (24) and the starting point in (28), P Nyquist impulses have to be considered for all corresponding positions in a period as for each position, different predistortion coefficients are found. This leads to a Nyquist impulse matrix $\boldsymbol{i}_\mathrm{LPTV}$ of size $(N_\mathrm{e}+N_\mathrm{h}-1)\times P$ containing the Nyquist conditions. At first, P columns $j \in \{j_0,\ldots,j_0+P-1\}$ within the inner matrix columns of $\boldsymbol{H}_\mathrm{LPTV}$ are chosen in a way that $j_0 \bmod P = 0$. Defining $\kappa = j \bmod P$, it holds $\kappa \in \{0,\ldots,P-1\}$. By definition, all impulse reactions $\tilde{h}\,[\rho,\nu]$ contain time-discrete pulses with a maximum at the same position ρ. Hence, the maxima of the sorted columns j appear with a row increment of one. I.e., for

$$\eta_\kappa = \underset{n\in\{0,\ldots,N_\mathrm{e}+N_\mathrm{h}-1\}}{\operatorname{argmax}} \left\{\hat{h}_j\,[n]\right\} \tag{31}$$

$$\underbrace{\begin{pmatrix} h[0] & 0 & \cdots & 0 \\ h[1] & h[0] & \cdots & \\ h[2] & h[1] & \ddots & \vdots \\ \vdots & \vdots & \cdots & \\ h[N_\mathrm{h}-2] & h[N_\mathrm{h}-3] & \cdots & 0 \\ h[N_\mathrm{h}-1] & h[N_\mathrm{h}-2] & \cdots & \boxed{h[0]} \\ 0 & h[N_\mathrm{h}-1] & \cdots & h[1] \\ 0 & 0 & \cdots & h[2] \\ \vdots & \vdots & \ddots & \vdots \\ 0 & 0 & \cdots & h[N_\mathrm{h}-1] \end{pmatrix}}_{\boldsymbol{H}} \cdot \underbrace{\begin{pmatrix} e[0] \\ e[1] \\ e[2] \\ \vdots \\ e[N_\mathrm{e}-1] \end{pmatrix}}_{\boldsymbol{e}} = \underbrace{\begin{pmatrix} 0 \\ 0 \\ \vdots \\ 0 \\ 1 \\ 0 \\ \vdots \\ 0 \\ 0 \end{pmatrix}}_{\boldsymbol{i}} + \underbrace{\begin{pmatrix} \epsilon_\mathrm{i}[0] \\ \epsilon_\mathrm{i}[1] \\ \vdots \\ \epsilon_\mathrm{i}[n_0-1] \\ \epsilon_\mathrm{i}[n_0] \\ \epsilon_\mathrm{i}[n_0+1] \\ \vdots \\ \epsilon_\mathrm{i}[N_\mathrm{h}+N_\mathrm{e}-3] \\ \epsilon_\mathrm{i}[N_\mathrm{h}+N_\mathrm{e}-2] \end{pmatrix}}_{\boldsymbol{\epsilon}_\mathrm{i}} \tag{24}$$

$$\boldsymbol{H}_\mathrm{LPTV} = \begin{pmatrix} \tilde{h}[0,0] & 0 & \dots & 0 & 0 & 0 & \dots & 0 \\ \tilde{h}[1,0] & \tilde{h}[0,1] & \dots & 0 & 0 & 0 & \dots & 0 \\ \tilde{h}[2,0] & \tilde{h}[1,1] & \dots & 0 & 0 & 0 & \dots & 0 \\ \vdots & \vdots & \ddots & \vdots & \vdots & \vdots & \ddots & \vdots \\ \tilde{h}[N_\mathrm{h}-2,0] & \tilde{h}[N_\mathrm{h}-3,1] & \dots & 0 & 0 & 0 & \dots & 0 \\ \tilde{h}[N_\mathrm{h}-1,0] & \tilde{h}[N_\mathrm{h}-2,1] & \dots & \boxed{\tilde{h}[0,P-1]} & 0 & 0 & \dots & 0 \\ 0 & \tilde{h}[N_\mathrm{h}-1,1] & \dots & \tilde{h}[1,P-1] & \tilde{h}[0,0] & 0 & \dots & 0 \\ 0 & 0 & \dots & \tilde{h}[2,P-1] & \tilde{h}[1,0] & \tilde{h}[0,1] & \dots & 0 \\ 0 & 0 & \dots & \tilde{h}[3,P-1] & \tilde{h}[2,0] & \tilde{h}[1,1] & \dots & 0 \\ \vdots & \vdots & \ddots & \vdots & \vdots & \vdots & \ddots & \vdots \\ 0 & 0 & \dots & 0 & 0 & 0 & \dots & \tilde{h}[N_\mathrm{h}-1,P-1] \end{pmatrix} \tag{29}$$

$$\boldsymbol{i}_\mathrm{LPTV} = \begin{array}{c} \begin{matrix} \boldsymbol{i}_0 & \boldsymbol{i}_1 & & \boldsymbol{i}_{P-1} \\ \downarrow & \downarrow & & \downarrow \end{matrix} \\ \begin{pmatrix} 0 & 0 & \cdots & 0 \\ \vdots & \vdots & \ddots & \vdots \\ 1 & 0 & \cdots & 0 \\ 0 & 1 & \cdots & 0 \\ \vdots & \vdots & \ddots & \vdots \\ 0 & 0 & \cdots & 1 \\ \vdots & \vdots & \ddots & \vdots \\ 0 & 0 & \cdots & 0 \end{pmatrix} \end{array} \begin{array}{l} \\ \\ \leftarrow \text{ row } \eta_0 \\ \leftarrow \text{ row } \eta_1 \\ \\ \leftarrow \text{ row } \eta_{P-1} \\ \\ \end{array} \tag{34}$$

it holds

$$\eta_{\kappa+1} = \eta_\kappa + 1 \ . \tag{32}$$

Thus, the P column vectors $\boldsymbol{i}_\kappa$ of the Nyquist impulse matrix $\boldsymbol{i}_\mathrm{LPTV}$ are defined by

$$\boldsymbol{i}_\kappa = (0, 0, \dots, 0, 1, 0, \dots, 0)^\mathrm{T} \tag{33}$$
$$\uparrow \text{ element } \eta_\kappa$$

where $(\cdot)^\mathrm{T}$ denotes the matrix transpose operator leading to the matrix given in (34). Combining the P equation systems

$$\boldsymbol{H}_\mathrm{LPTV} \cdot \boldsymbol{e}_{\mathrm{LPTV},\,\kappa} = \boldsymbol{i}_\kappa + \boldsymbol{\epsilon}_{\mathrm{i},\,\kappa} \tag{35}$$

results in

$$\boldsymbol{H}_\mathrm{LPTV} \cdot \boldsymbol{e}_\mathrm{LPTV} = \boldsymbol{i}_\mathrm{LPTV} + \boldsymbol{\epsilon}_{\mathrm{i,\,LPTV}} \tag{36}$$

with

$$\boldsymbol{e}_\mathrm{LPTV} = \left(\boldsymbol{e}_{\mathrm{LPTV},\,0}, \boldsymbol{e}_{\mathrm{LPTV},\,1}, \dots, \boldsymbol{e}_{\mathrm{LPTV},\,P-1}\right) \in \mathbb{R}^{N_\mathrm{e} \times P} \ , \tag{37a}$$

$$\boldsymbol{i}_\mathrm{LPTV} = \left(\boldsymbol{i}_0, \boldsymbol{i}_1, \dots, \boldsymbol{i}_{P-1}\right) \in \mathbb{R}^{(N_\mathrm{e}+N_\mathrm{h}-1) \times P} \quad \text{and} \tag{37b}$$

$$\boldsymbol{\epsilon}_{\mathrm{i,\,LPTV}} = \left(\boldsymbol{\epsilon}_{\mathrm{i},\,0}, \boldsymbol{\epsilon}_{\mathrm{i},\,1}, \dots, \boldsymbol{\epsilon}_{\mathrm{i},\,\mathrm{P}-1}\right) \in \mathbb{R}^{(N_\mathrm{e}+N_\mathrm{h}-1) \times P} \ . \tag{37c}$$

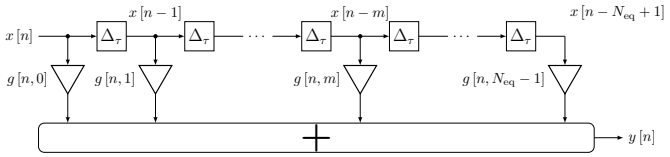

Fig. 6. Discrete-time, time-varying finite impulse response filter for LPTV predistortion [11].

Again, this is an overdetermined system and the LS approach from (26) is applied:

$$\begin{aligned}\boldsymbol{e}_{\mathrm{LPTV,\,LS}} &= \left(\boldsymbol{e}_{\mathrm{LPTV,\,LS},\,0}, \boldsymbol{e}_{\mathrm{LPTV,\,LS},\,1}, \ldots, \boldsymbol{e}_{\mathrm{LPTV,\,LS},\,P-1}\right) \\ &= \left(\boldsymbol{H}_{\mathrm{LPTV}}^{\mathrm{H}}\, \boldsymbol{H}_{\mathrm{LPTV}}\right)^{-1} \boldsymbol{H}_{\mathrm{LPTV}}^{\mathrm{H}}\, \boldsymbol{i}_{\mathrm{LPTV}}\ . \end{aligned} \tag{38}$$

The calculations are restricted to one period P and the result can be easily extended to any length using a periodic continuation $\tilde{\boldsymbol{e}}_{\mathrm{PLTV,\,LS}}$ of the predistortion coefficients $\boldsymbol{e}_{\mathrm{PLTV,\,LS}}$ with the property

$$\tilde{e}_{\mathrm{LPTV,\,LS}}\left[i + z_0 P, j + z_0 P\right] = \tilde{e}_{\mathrm{LPTV,\,LS}}\left[i, j\right] \tag{39}$$

for $z_0 \in \mathbb{Z}$.

For practical implementations, the modified impulse response $g_{\mathrm{eq}}\left[n, \mu\right]$ is more convenient for calculations. The transition to $g_{\mathrm{eq}}\left[n, \mu\right]$ is given in (40).

$$g_{\mathrm{eq}}\left[n, \mu\right] = \begin{cases} \tilde{e}_{\mathrm{LPTV,\,LS}}\left[n, n-\mu\right] & \text{for } 0 \le \mu \le N_{\mathrm{eq}} - 1\ , \\ 0 & \text{otherwise}\ . \end{cases} \tag{40}$$

In (40), the filter length $N_{\mathrm{eq}} \le N_{\mathrm{e}}$ is introduced. Depending on the application and conditions, it can differ in its length from N_{e}. Obviously, it holds

$$g_{\mathrm{eq}}\left[n + z_0 P, \mu\right] = g_{\mathrm{eq}}\left[n, \mu\right] \tag{41}$$

for $0 \le \mu \le N_{\mathrm{eq}} - 1$ and $z_0 \in \mathbb{Z}$ as expected. Due to its simpler periodic structure, it is favorable to use $g_{\mathrm{eq}}\left[n, \mu\right]$ for predistortion even though $\tilde{\boldsymbol{e}}_{\mathrm{PLTV,\,LS}}$ can be used, too. All filter coefficients are given in a $(P \times N_{\mathrm{eq}})$ matrix which can be accessed by $g_{\mathrm{eq}}\left[\left(n \bmod P\right), \mu\right]$. Predistortion $\tilde{y}_{\mathrm{eq}}\left[n\right]$ of data $x\left[n\right]$ of length N_{d} can be performed according to (42) either by using $\tilde{e}_{\mathrm{LPTV,\,LS}}\left[n, \nu\right]$ or by using $g_{\mathrm{eq}}\left[n, \mu\right]$ exploiting the respective periodicity.

$$\begin{aligned}\tilde{y}_{\mathrm{eq}}\left[n\right] &= \sum_{\nu=n-N_{\mathrm{eq}}+1}^{n} x\left[\nu\right] \tilde{e}_{\mathrm{LPTV,\,LS}}\left[n, \nu\right] \\ &\overset{\mu=n-\nu}{=\!=} \sum_{\mu=0}^{N_{\mathrm{eq}}-1} x\left[n-\mu\right] g_{\mathrm{eq}}\left[\left(n \bmod P\right), \mu\right] \\ &= x\left[n\right] \circledast g_{\mathrm{eq}}\left[\left(n \bmod P\right), \mu\right]\ . \end{aligned} \tag{42}$$

The corresponding filter structure for the case of $g_{\mathrm{eq}}\left[n, \mu\right]$ is shown in Fig. 6 revealing a transversal time-discrete, time-varying filter with finite impulse response. Compared to an LTI filter, only a slight adaption is required. Instead of a vector containing the filter coefficients, a matrix with coefficients $g_{\mathrm{eq}}\left[\left(n \bmod P\right), \mu\right]$ is applied. I.e., a lookup table of size $P \times N_{\mathrm{eq}}$ is required instead of $1 \times N_{\mathrm{eq}}$.

Finally, a normalization step to full-scale $[-1, 1]$ according to (43) is applied.

$$y_{\mathrm{eq}}\left[n\right] = \frac{\tilde{y}_{\mathrm{eq}}\left[n\right]}{\max\limits_{0 \le n \le N_{\mathrm{d}}-1} \left\{\left|\tilde{y}_{\mathrm{eq}}\left[n\right]\right|\right\}}\ . \tag{43}$$

Additionally, quantization is required to map the data to the digital code.

Predistortion based on (42) considering deterministic LPTV effects is a universal predistortion method and reveals massive cancellation of LPTV distortions described in Section III. It has to be mentioned that the state of the circuit during system identification differs from the state during transmission experiments due to substantial difference in the signals concerning the number of transitions. This might require a readjustment of the operation parameters. Finally, a defined starting behavior of the AWG is a prerequisite for this predistortion method in order to ensure that the position of each sample is properly correlated to the system's state. The sample positions of the predistorted data signals have to correspond to the appropriate impulse reactions during system identification. I.e., the sample of a dedicated memory position always has to arrive at the output at the same clock network state. As the AWG is stopped between system identification and the output of the predistorted data, a defined starting behavior ensures the alignment of the proper filter coefficients to the sample's memory position. This is realized by internal sampling of the starting trigger signal.

Fig. 7 summarizes the procedure of system identification (1. and 2.) and LPTV predistortion in case of offline preprocessing for an AWG (3a. and 4a.) as well as in case of real-time processing in a transmitter (Tx) using a digital signal processor (DSP, 3b). The AWG measurement results of this work are generated following the procedure 1. to 4a. In case of a real-time implementation, the DSP has to implement the filter of Fig. 6 with periodically changing filter coefficients stored in a two-dimensional lookup table of size $P \times N_{\mathrm{eq}}$.

VII. Measurement Results

For measurements, a subsampling oscilloscope with a sampling module input bandwidth of 70 GHz in combination with a phase reference module driven by the $f_{\mathrm{s}}/2$ clock for low jitter measurements (< 100 fs RMS) is used. A half-rate clock signal is splitted into two parts. One part is used to drive the phase reference module and the other part drives the circuit. The measurement setup is illustrated in Fig. 8. Due to this setup, two eye openings have to be considered in the analysis of eye diagrams. As sampling frequencies, $f_{\mathrm{s}} = 64\,\mathrm{GS/s}$, $f_{\mathrm{s}} = 80\,\mathrm{GS/s}$ and $f_{\mathrm{s}} = 100\,\mathrm{GS/s}$ are chosen. In the following, two types of signals are considered and investigated separately: single-tone signals and broadband PAM signals. At first, the system's impulse response is examined.

A. Estimation of the Impulse Response

According to Section VI-C, an estimation of the impulse response including the chip as well as the whole measurement environment is obtained by the responses to impulses at

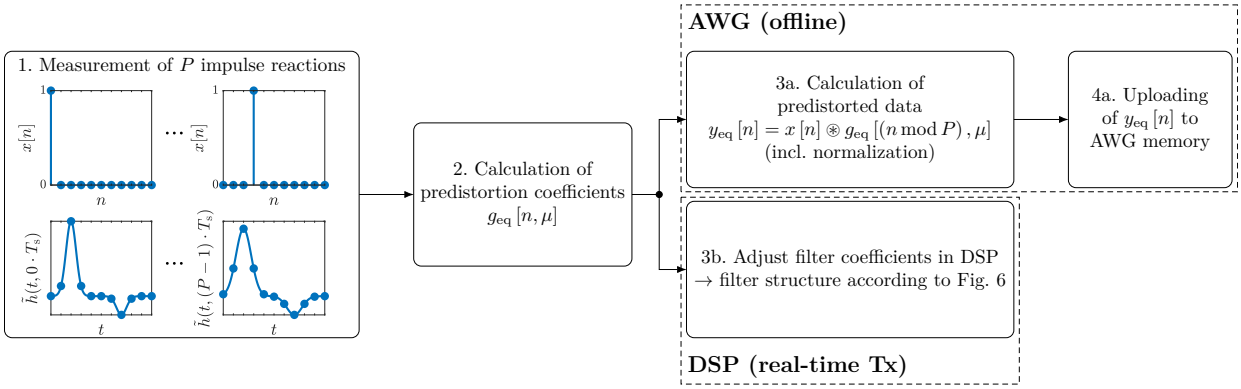

Fig. 7. Procedure of system identification (1. and 2.) and LPTV predistortion (3a., 4a. or 3b., respectively).

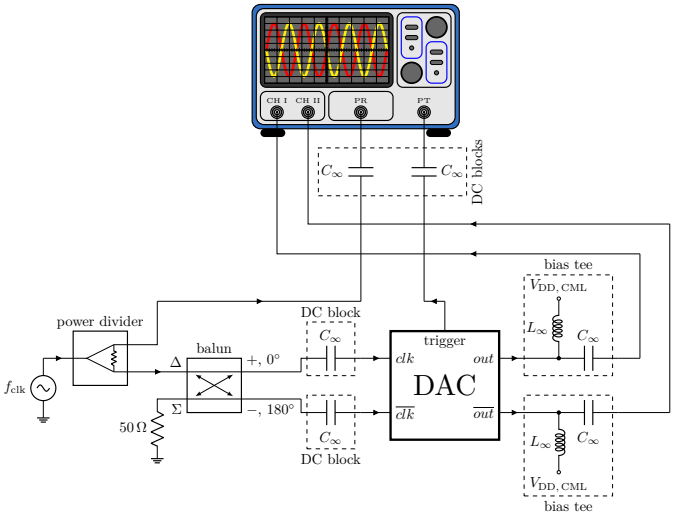

Fig. 8. Measurement setup (PR: phase reference, PT: prescale trigger) [21].

different corresponding positions in a period P. It includes all the circuit itself, the chip assembly as well as the components of the measurement setup in the output path. In Fig. 9, the differential voltages $V_{\tilde{h},\mathrm{d}}(t, \nu T_s)$ and $V_{h,\mathrm{d}}(t, \nu T_s)$ corresponding to $\tilde{h}(t, \nu T_s)$ and $h(t, \nu T_s)$, respectively, are shown at $f_s = 100\,\mathrm{GS/s}$ representing the raw measurement data without normalization. Furthermore, transfer functions $V_{\tilde{H},\mathrm{d}}$ calculated from $V_{\tilde{h},\mathrm{d}}(t, \nu T_s)$ are given in Fig. 9b. The measurement results reveal different aspects. For simplification, the results of only one period are shown but the repetition of impulse reactions with $P = 32$ is verified experimentally. Fig. 9a shows that the occuring LPTV effects can be described by a combination of deterministic clock jitter as well as periodic gain variations as described in Section III. Pulse widths as well as pulse heights vary inside one period. Moreover, reflections can be observed $\sim 170\,\mathrm{ps}$ after the impulses which are also considered in the predistortion which is why a filter length of $N_{eq} = 32$ is chosen. Without considering reflections, much shorter filter lengths (e.g. $N_{eq} = 6$) are sufficient. The choice of the number of coefficients can be evaluated with the help of Fig. 9a depending on the length of the reaction.

In Fig. 9c, similarities between impulse reactions at shorter periods $P_0 = 16$ and $P_1 = 8$ can be observed suggesting the assumption of dominating effects due to $f_s/8$ and $f_s/16$ domains (and $f_s/4$). Hence, accepting larger tolerances, also reduced periods P are applicable for predistortion. As offline pre-processing is used for predistortion and the filter length is not a critical factor here, a generous filter length of $N_{eq} = 32$ coefficients and the maximum period of $P = 32$ are used for demonstration in the following. However, the number of significant predistortion coefficients is well below. Finally, consecutive pairs of pulses show significant similarities supporting the assumption that LPTV artifacts are dominated by the CMOS sub-DACs and not by the current-mode AMUX. Current-mode topology of the AMUX and the respective clock path features a constant load to supply voltage in contrast to the sub-DAC implementation essentially based on static CMOS logic.

B. Single-Tone Signals

The impact of LPTV predistortion on single-tone signals is discussed in the following. The results are determined by taking the DFT of the equivalent-time output samples captured by the oscilloscope across one data period. To separate the signal part and distortions from pure random noise, an averaged x_{SD} and a non-averaged time-domain measurement is performed and the noise part x_N is determined by subtracting the two measurements. Fig. 10 compares the spectra at $f_s = 64\,\mathrm{GS/s}$ and $f_s = 100\,\mathrm{GS/s}$ with and without LPTV predistortion for signal frequencies f_{sig} close to half of the respective Nyquist frequency with dedicated spurious components being highlighted. As $SNDR$ values are dominated by distortions, signal-to-distortion ratio (SDR) values are considered. Significant improvement in the SDR as well as in the spurious free dynamic range ($SFDR$) can be observed by considerable reduction of LPTV spurious components according to (16) and (20). An LTI predistortion is not able to compensate these LPTV effects. Spurious components in the spectra without predistortion resulting from spectral replica at multiples of $1/(P \cdot T_s)$ can be observed which is in accordance with theoretical expectations. Components for $P_1 = 8$ and $P_2 = 4$ are most prominent indicating that the assumed period of

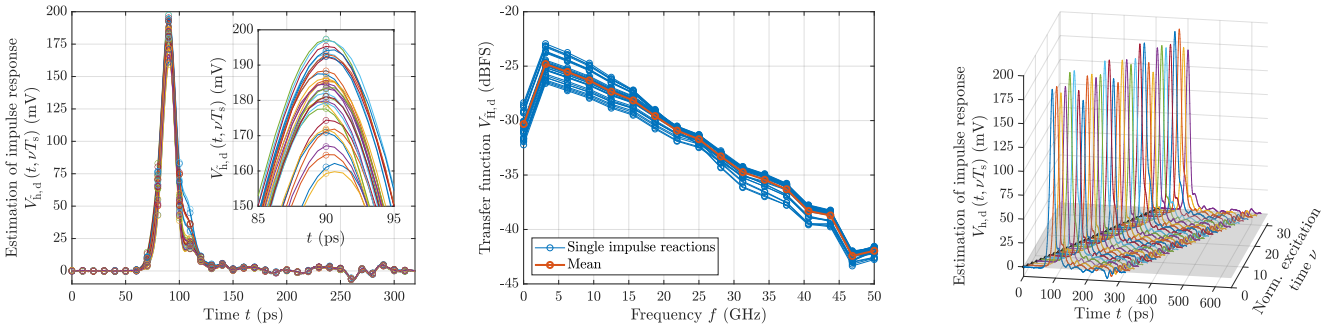

Fig. 9. Impulse reactions to single pulse stimulus at different pulse positions mapped to one period of $P = 32$ at $f_\mathrm{s} = 100\,\mathrm{GS/s}$ (differential measurements). (a) Measurement results corresponding to $\tilde{h}\,(t, \nu T_\mathrm{s})$. The sampling points considered for predistortion are marked. (b) Transfer functions of the different impulse reactions in (a) normalized to full-scale. (c) Measurement results corresponding to $h\,(t, \nu T_\mathrm{s})$. Measurement results represent the mean value of a positive and a negative impulse at corresponding positions averaging asymmetries.

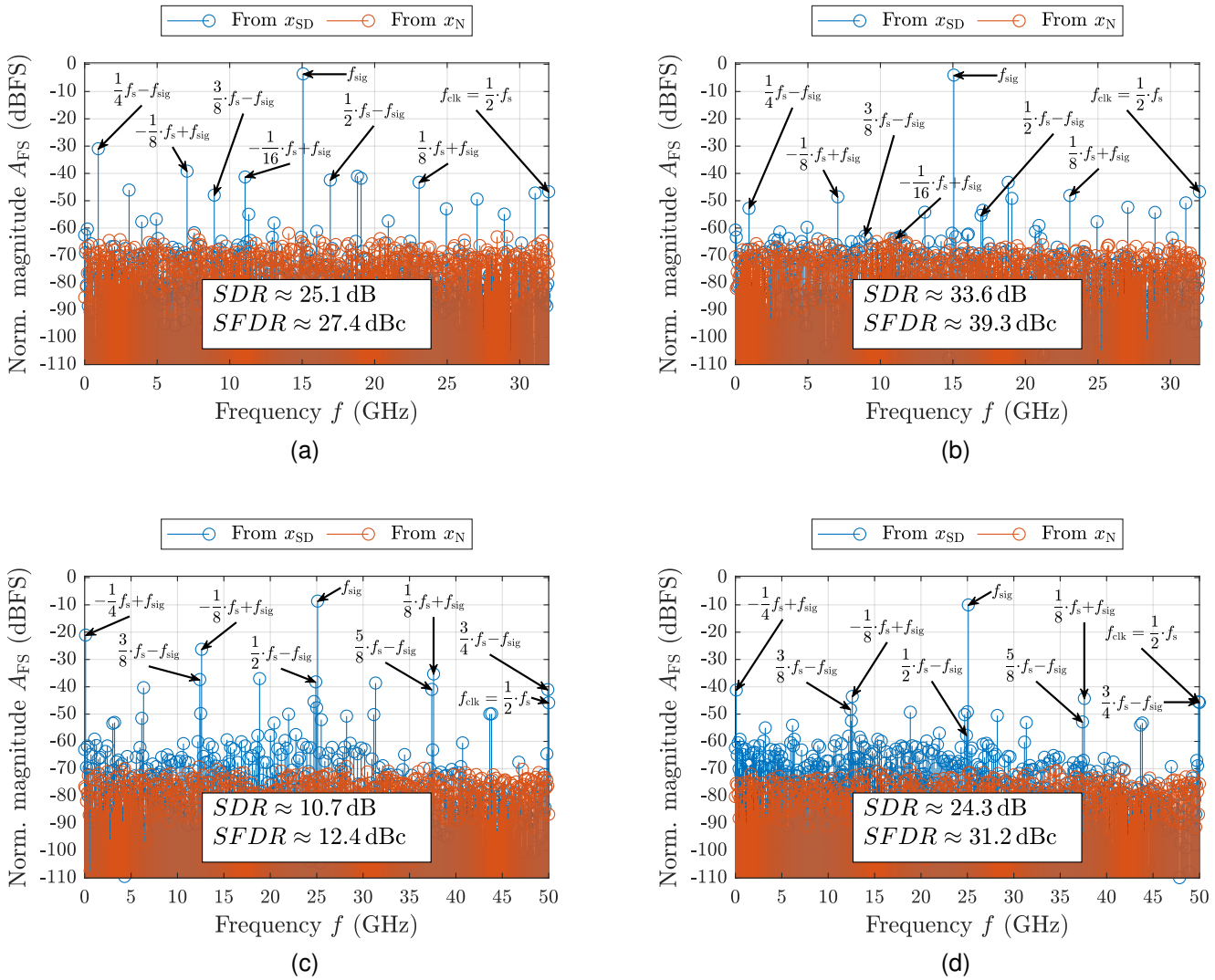

Fig. 10. Output spectra with dedicated spurious components being highlighted normalized to full-scale. $f_\mathrm{s} = 64\,\mathrm{GS/s}$, $f_\mathrm{sig} \approx 15\,\mathrm{GHz}$ (a) without and (b) with predistortion as well as $f_\mathrm{s} = 100\,\mathrm{GS/s}$, $f_\mathrm{sig} \approx 25\,\mathrm{GHz}$ (c) without and (d) with predistortion. In all measurements, a clock feed-through is also visible. Spectra are calculated from the averaged signal x_SD (signal and distortion part) and from x_N (pure random noise part).

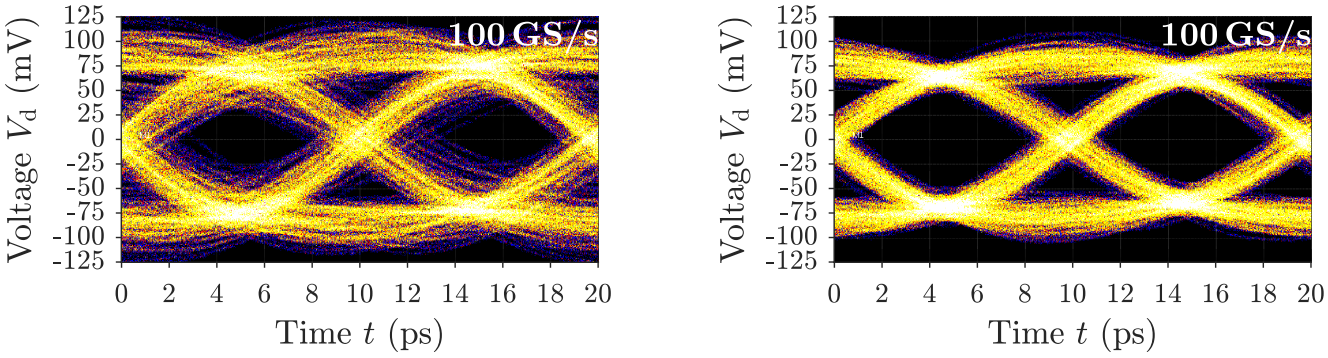

(a) $SNDR$: $\sim 13.7\,\mathrm{dB}/\sim 13.4\,\mathrm{dB}$ (b) $SNDR$: $\sim 20.7\,\mathrm{dB}/\sim 19.2\,\mathrm{dB}$

Fig. 11. Measured PAM eye diagrams comparing LTI predistortion to LPTV predistortion (differential signals). (a) $f_\mathrm{s} = 100\,\mathrm{GS/s}$ PAM-2 with LTI predistortion and (b) $f_\mathrm{s} = 100\,\mathrm{GS/s}$ PAM-2 with LPTV predistortion. $SNDR$ values are given for both eye openings.

TABLE I
COMPARISON OF $SNDR$ VALUES WITHOUT AND WITH LPTV PREDISTORTION EXTRACTED FROM SINGLE-TONE MEASUREMENTS FOR DIFFERENT SAMPLING RATES AND DIFFERENT SIGNAL FREQUENCIES.

Sampling rate f_s (GS/s)	Frequency f_sig (GHz)	$SNDR$ w/o predistortion (dB)	$SNDR$ w. predistortion (dB)
64	~ 1	35.9	36.0 (+0.1 dB)
64	~ 15	24.9	32.8 (+7.9 dB)
64	~ 32	24.4	28.2 (+3.8 dB)
100	~ 1	33.9	33.7 (−0.2 dB)
100	~ 25	10.7	24.2 (+13.5 dB)
100	~ 50	22.6	21.2 (−1.4 dB)

$P = 32$ is chosen generously. As components corresponding to $P_3 = 2$ are less significant, the AMUX contribution to LPTV distortions reveals to be less than the distortions from the sub-DACs as expected from circuit topology considerations in Section V. An important aspect of the predistortion concept is that the signal magnitude is hardly affected which is demonstrated in Fig. 10. In Table I, the effect of LPTV predistortion on $SNDR$ values at different frequencies is summarized. As the main contribution to the LPTV behavior is determined by the sub-DACs, the impact of LPTV effects on the spectra is different for different signal frequencies and hence the one of the LPTV predistortion as well. At $f_\mathrm{sig} \approx f_\mathrm{s}/4$, the sub-DACs rapidly change their outputs which is why LPTV behavior has the highest impact.

C. PAM Signals

Furthermore, the influence of LPTV predistortion on time-domain modulation experiments is investigated. As comparing quantity, $SNDR$ values are calculated from the histograms of broadband PAM signals in the maximum eye openings with 100 acquisitions. The pattern lengths are 1024 symbols each. In Fig. 11, the results of LTI predistortion with a single (mean) impulse reaction according to Section VI-B is compared to LPTV predistortion for a PAM-2 signal at $f_\mathrm{s} = 100\,\mathrm{GS/s}$. Significant $SNDR$ improvement of $\sim$ 6-7 dB can be observed due to LPTV predistortion.

For broadband PAM signals, also the training sequence based approach of Section VI-A is a meaningful predistortion method. However, it is not a universal concept in presence of LPTV effects. It delivers the inverse channel response based on a particular data sequence which is suitable for predistortion of the same base data sequence $x\,[n]$. Applying an inverse channel impulse response estimated from a sequence $x_1\,[n]$ to a sequence $x_2\,[n] \neq x_1\,[n]$ features an LTI method and leads to similar results as method VI-B. Hence, in LPTV systems, this method is only powerful for broadband signals where the training and the target data sequence are identical not being suitable for transmission applications. In this case, the method can be used as reference to evaluate the LPTV predistortion of this work. Fig. 12 compares training based predistortion to universal LPTV predistortion for $f_\mathrm{s} = 80\,\mathrm{GS/s}$ and $f_\mathrm{s} = 100\,\mathrm{GS/s}$. It becomes obvious that the LPTV predistortion leads to equivalent results. Considering the disadvantages of the training method, such as the constraint to broadband signals and the requirement of the same data sequence for training and predistortion, the LPTV predistortion advantage predominates.

In summary, the LPTV predistortion method based on system identification by shifted unit impulses is a powerful and universal concept to compensate LPTV artifacts in interleaved DACs. It can be applied to both single-tone or narrowband signals and broadband signals. Reference results of broadband signals based on predistortion with identical training and target data can be attained by LPTV predistortion.

VIII. CONCLUSION

LPTV distortions in DACs due to interleaving or periodic artifacts can have significant influence on the analog output signals and deteriorate signal quality. Particularly, CMOS implementations providing a high, dynamic load to the supply voltage are susceptible to distortions for topological reasons. To compensate for these effects, a universal LPTV predistortion method in time domain based on system identification by

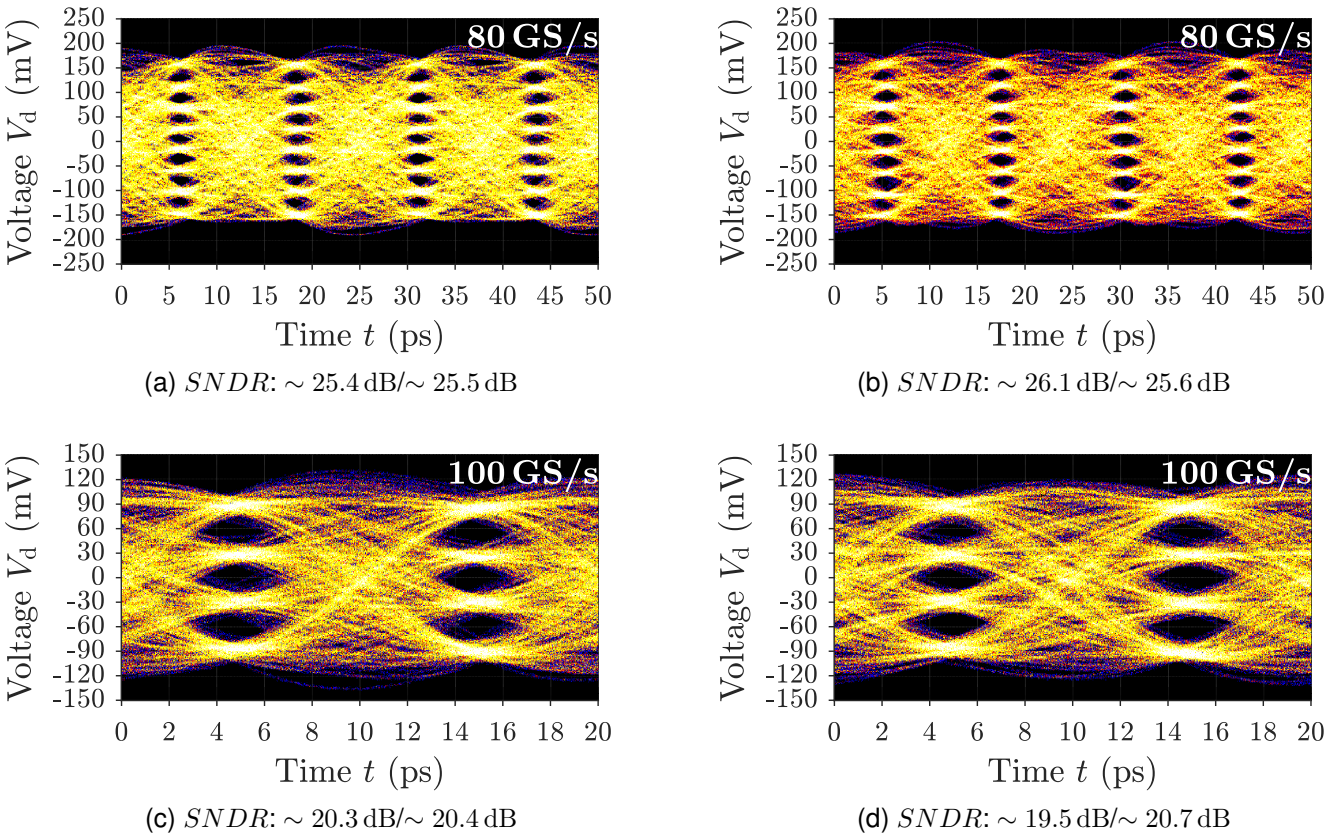

Fig. 12. Measured PAM eye diagrams comparing predistortion based on training sequence and identical target sequence to LPTV predistortion (differential signals). (a) $f_\mathrm{s} = 80\,\mathrm{GS/s}$ PAM-8 based on training sequence, (b) $f_\mathrm{s} = 80\,\mathrm{GS/s}$ PAM-8 based on LPTV predistortion, (c) $f_\mathrm{s} = 100\,\mathrm{GS/s}$ PAM-4 based on training sequence and (d) $f_\mathrm{s} = 100\,\mathrm{GS/s}$ PAM-4 based on LPTV predistortion. $SNDR$ values are given for both eye openings.

shifted unit impulses is proposed. Once the system is characterized, the method can be directly translated to a classical transversal filter which only differs from LTI filters by a two-dimensional filter coefficient matrix instead of constant coefficients. Compared to other MIMO/MISO methods with frequency-domain operations [8]–[10] that might be a drawback for real-time systems, the predistortion concept shown here is applicable to real-time implementations. Generally, it can be applied to any time-interleaved system with monolithic or hybrid implementation. A period of $P = 32$ is shown experimentally for the presented time-interleaved DAC and the predistortion method is applied to it. In systems with shorter periods P, e.g. 2:1 systems where P is only 2, hardly more filter effort ($2 \times N_\mathrm{eq}$ coefficients) is required compared to LTI systems ($1 \times N_\mathrm{eq}$ coefficients). Measurement results are given up to $f_\mathrm{s} = 100\,\mathrm{GS/s}$ with significant improvement of $SNDR$. In single-tone measurements at $f_\mathrm{s} = 100\,\mathrm{GS/s}$, $SNDR$ improvement of up to 13.5 dB can be shown. Additionally, equivalent results compared to predistortion with identical training and target data are demonstrated for broadband PAM signals at $f_\mathrm{s} = 80\,\mathrm{GS/s}$ (PAM-8) and $f_\mathrm{s} = 100\,\mathrm{GS/s}$ (PAM-4). The observation of periodic behavior in the DAC output signal is in accordance with an inherent conceptual period in the system's architecture and might be attributed to a dynamic load to supply voltage with a periodic pattern. Further development could be to estimate the two-dimensional impulse response from more complex signals to adapt the state of the circuit during system identification to the one during data transmission experiments.

Appendix
Derivation of the DAC Output Spectrum for Periodic, Nonuniform ZOH Behavior

Generally, timing mismatch effects can be represented by three processes [19]:

1) The input signal is sampled nonuniformly and the output signal is a uniform sequence.
2) The input signal is sampled uniformly and the output signal has a nonuniform holding waveform.
3) The input signal is sampled nonuniformly and the output signal has a nonuniform holding waveform with time correlation to the input.

As a common result, distortions in the output signal occur. Below, the second case is considered to describe a DAC output signal with periodic, nonuniform ZOH behavior which is illustrated in Fig. 1. To show these effects analytically, the results of the model according to [17]–[20] shall be given in this paragraph assuming a jittered clock. Let $\{t_n\}$ be a sequence of points in time with

$$t_n = nT_\mathrm{s} + \Delta_n \tag{44}$$

where n is an integer, T_s is the nominal sampling period and Δ_n is a deterministic, periodic sequence of time values with period $P \cdot T_\mathrm{s}$ representing the jitter contribution. Thus, P is the normalized period. It holds

$$P = n_\mathrm{j} T_\mathrm{j} / T_\mathrm{s} \tag{45}$$

with the jitter period T_j and n_j represents the smallest natural number to make P a natural number. Substituting $n = \nu P + p$ with $\nu \in \mathbb{Z}$ and $p \in \{0, \ldots, P-1\}$, t_n can be rewritten as (46).

$$\begin{aligned} t_n &= (\nu P + p)\, T_\mathrm{s} + \Delta_{\nu P + p} = \nu P T_\mathrm{s} + p T_\mathrm{s} + \Delta_p \\ &= \nu P T_\mathrm{s} + p T_\mathrm{s} + r_p T_\mathrm{s} \end{aligned} \tag{46}$$

The variable $r_p = \Delta_p / T_\mathrm{s}$ describes the relative timing skew. The model of nonuniform ZOH behavior can be described by (47) considering the substitution in (46).

$$\begin{aligned} y(t) &= \sum_{n=-\infty}^{\infty} x(n T_\mathrm{s})\, h_n(t - t_n) \\ &= \sum_{p=0}^{P-1} \sum_{\nu=-\infty}^{\infty} x(\nu P T_\mathrm{s} + p T_\mathrm{s})\, h_p(t - \nu P T_\mathrm{s} - p T_\mathrm{s} - r_p T_\mathrm{s}) \end{aligned} \tag{47}$$

The nonuniform holding outputs are represented by rectangular functions

$$h_p(t) = s(t) - s(t - T_\mathrm{s} - r_{p+1} T_\mathrm{s} + r_p T_\mathrm{s}) \tag{48}$$

starting from $t = 0$ to $t = T_\mathrm{s} + r_{p+1} T_\mathrm{s} - r_p T_\mathrm{s}$ and having a height of 1. They correspond to the definition of $\tilde{h}(\rho, \tau)$ in (7). The function $s(t)$ describes the Heaviside step function (unit step function). Applying the Fourier transform to (47) yields [19], [20]

$$\begin{aligned} Y(\mathrm{j}\omega) =& \frac{1}{P T_\mathrm{s}} \sum_{\nu=-\infty}^{\infty} \sum_{p=0}^{P-1} H_p(\mathrm{j}\omega)\, \mathrm{e}^{-\mathrm{j}\frac{2\pi}{P}\nu p}\, \mathrm{e}^{-\mathrm{j}\omega r_p T_\mathrm{s}} \\ & \cdot X\left(\mathrm{j}\omega - \mathrm{j}\nu \frac{2\pi}{P T_\mathrm{s}}\right) \\ =& \frac{1}{P T_\mathrm{s}} \sum_{\nu=-\infty}^{\infty} A_\nu(\mathrm{j}\omega)\, X\left(\mathrm{j}\omega - \mathrm{j}\nu \frac{2\pi}{P T_\mathrm{s}}\right) \end{aligned} \tag{49}$$

with

$$A_\nu(\mathrm{j}\omega) = \sum_{p=0}^{P-1} H_p(\mathrm{j}\omega)\, \mathrm{e}^{-\mathrm{j}\frac{2\pi}{P}\nu p}\, \mathrm{e}^{-\mathrm{j}\omega r_p T_\mathrm{s}} \tag{50a}$$

$$\begin{aligned} =& \sum_{p=0}^{P-1} \frac{2 \cdot \sin\left(\omega\left(1 + r_{p+1} - r_p\right) T_\mathrm{s}/2\right)}{\omega} \\ & \cdot \mathrm{e}^{-\mathrm{j}\omega(1 + r_{p+1} - r_p) T_\mathrm{s}/2}\, \mathrm{e}^{-\mathrm{j}\omega r_p T_\mathrm{s}}\, \mathrm{e}^{-\mathrm{j}\frac{2\pi}{P}\nu p}\,. \end{aligned} \tag{50b}$$

REFERENCES

[1] F. Buchali, "Beyond 1 Tbit/s transmission using high-speed DACs and analog multiplexing," in *2021 Optical Fiber Communications Conference and Exhibition (OFC)*, 2021.

[2] F. Buchali, V. Lauinger, M. Chagnon, K. Schuh, and V. Aref, "CMOS DAC Supported 1.1 Tb/s/λ DWDM Transmission at 9.8 bit/s/Hz Over DCI Distances," *J. Lightw. Technol.*, vol. 39, no. 4, pp. 1171–1178, 2021.

[3] F. Buchali *et al.*, "128 GSa/s SiGe DAC Implementation Enabling 1.52 Tb/s Single Carrier Transmission," *J. Lightw. Technol.*, vol. 39, no. 3, pp. 763–770, 2021.

[4] J. Kim *et al.*, "8.1 A 224Gb/s DAC-Based PAM-4 Transmitter with 8-Tap FFE in 10nm CMOS," in *2021 IEEE International Solid-State Circuits Conference (ISSCC)*, 2021, pp. 126–128.

[5] J. Kim *et al.*, "A 224-Gb/s DAC-Based PAM-4 Quarter-Rate Transmitter With 8-Tap FFE in 10-nm FinFET," *IEEE J. Solid-State Circuits*, vol. 57, no. 1, pp. 6–20, 2022.

[6] T. O. Dickson *et al.*, "A 72-GS/s, 8-Bit DAC-Based Wireline Transmitter in 4-nm FinFET CMOS for 200+ Gb/s Serial Links," *IEEE J. Solid-State Circuits*, pp. 1–13, 2022.

[7] T. Tannert *et al.*, "A SiGe-HBT 2:1 Analog Multiplexer with more than 67 GHz Bandwidth," in *2017 IEEE Bipolar/BiCMOS Circuits and Technology Meeting (BCTM)*, 2017, pp. 146–149.

[8] C. Schmidt, *Interleaving Concepts for Digital-to-Analog Converters – Algorithms, Models, Simulations and Experiments*, 1st ed. Wiesbaden: Springer Vieweg, 2020.

[9] C. Schmidt *et al.*, "120 GBd SiGe-Based 2:1 Analog Multiplexer Module for Ultra-Broadband Transmission Systems," in *2021 16th European Microwave Integrated Circuits Conference (EuMIC)*, 2022, pp. 169–172.

[10] J. Schostak *et al.*, "150 GBd PAM-4 Electrical Signal Generation using SiGe-Based Analog Multiplexer IC," in *2022 17th European Microwave Integrated Circuits Conference (EuMIC)*, 2022, pp. 173–176.

[11] J. Speidel, *Introduction to Digital Communications*, 2nd ed., ser. Signals and Communication Technology. Cham: Springer Nature Switzerland AG, 2021.

[12] P. A. Bello, "Characterization of Randomly Time-Variant Linear Channels," *IEEE Transactions on Communications Systems*, vol. 11, no. 4, pp. 360–393, 1963.

[13] S. Pavan and R. S. Rajan, "Interreciprocity in Linear Periodically Time-Varying Networks With Sampled Outputs," *IEEE Trans. Circuits Syst. II*, vol. 61, no. 9, pp. 686–690, 2014.

[14] S. Pavan, "On Linear Periodically Time Varying (LPTV) Systems with Modulated Inputs, and their Application to Smoothing Filters," in *2017 IEEE International Symposium on Circuits and Systems (ISCAS)*, 2017.

[15] A. Mehr and T. Chen, "Representations of Linear Periodically Time-Varying and Multirate Systems," *IEEE Trans. Signal Process.*, vol. 50, no. 9, pp. 2221–2229, 2002.

[16] C. Vogel and C. Krall, "Compensation of Distortions Caused by Periodic Nonuniform Holding Signals," in *2008 6th International Symposium on Communication Systems, Networks and Digital Signal Processing*, 2008, pp. 152–155.

[17] Y.-C. Jenq, "Digital-to-Analog (D/A) Converters with Nonuniformly Sampled Signals," *IEEE Trans. Instrum. Meas.*, vol. 45, no. 1, 1996.

[18] Y.-C. Jenq, "Direct Digital Synthesizer with Jittered Clock," *IEEE Trans. Instrum. Meas.*, vol. 46, no. 3, 1997.

[19] S.-P. U, S.-W. Sin, and R. Martins, "Exact Spectra Analysis of Sampled Signals With Jitter-Induced Nonuniformly Holding Effects," *IEEE Trans. Instrum. Meas.*, vol. 53, no. 4, 2004.

[20] L. Angrisani and M. D'Arco, "Modeling Timing Jitter Effects in Digital-to-Analog Converters," *IEEE Trans. Instrum. Meas.*, vol. 58, no. 2, 2009.

[21] D. Widmann, T. Tannert, X.-Q. Du, T. Veigel, M. Grözing, and M. Berroth, "A Time-Interleaved Digital-to-Analog Converter up to 118 GS/s with Integrated Analog Multiplexer in 28-nm FD-SOI CMOS Technology," *submitted to IEEE Journal of Solid-State Circuits*, 2023.

[22] J. Deveugele and M. Steyaert, "A 10-bit 250-MS/s Binary-Weighted Current-Steering DAC," *IEEE J. Solid-State Circuits*, vol. 41, no. 2, pp. 320–329, 2006.

[23] X. Wu, P. Palmers, and M. S. J. Steyaert, "A 130 nm CMOS 6-bit Full Nyquist 3 GS/s DAC," *IEEE J. Solid-State Circuits*, vol. 43, no. 11, pp. 2396–2403, 2008.

[24] B. Razavi, *Design of Integrated Circuits for Optical Communications*, 1st ed., ser. McGraw-Hill Higher Education. Boston: McGraw-Hill, 2003.

[25] J. G. Proakis and M. Salehi, Eds., *Digital Communications*, 5th ed., ser. McGraw-Hill higher education. Boston, [Mass.]: McGraw-Hill, 2008.

[26] K.-D. Kammeyer and A. Dekorsy, *Nachrichtenübertragung*, 6th ed. Springer Vieweg, 2018.

Daniel Widmann received the B.Sc. degree as well as the M.Sc. degree in electrical engineering and information technology from the University of Stuttgart, Germany. In 2016, he joined the Institute of Electrical and Optical Communications Engineering at the University of Stuttgart as a research staff member and is currently pursuing the Ph.D. degree. His research interests include the design of mixed-signal integrated CMOS circuits with an emphasis on high-speed digital-to-analog converters in CMOS technology.

Markus Grözing (Member, IEEE) received the Dipl.-Ing. and Dr.-Ing. degrees from the University of Stuttgart, Stuttgart, Germany, in 2000 and 2007, respectively. During his studies, he spent a year abroad at NTNU in Trondheim, Norway and worked at Infineon Technologies in Munich. His doctoral study was focused on phase noise and jitter in ring oscillators and mixed-signal CMOS circuit design. Since 2007, he has been leading the Integrated Circuit Design Group, Institute of Electrical and Optical Communications Engineering, University of Stuttgart. His current research topics are high-speed analog and mixed-signal circuits and neural networks, high-speed transmitters and receivers for serial links, and gigasample-range analog-to-digital and digital-to-analog converters in CMOS and BiCMOS technologies. He has authored or coauthored more than 100 scientific papers. Dr. Grözing has served as a Reviewer for the IEEE Transactions on Microwave Theory and Techniques (T–MTT), the IEEE Journal of Solid-State Circuits (JSSC), the IEEE Transactions on Circuits and Systems—II: Express Briefs (TCAS–II), the IEEE Transactions on Very Large Scale Integration (VLSI) Systems, the IEEE Journal of Lightwave Technology (JLT), and the IEEE Solid-State Circuits Letters (SSC-L).

Manfred Berroth (Senior Member, IEEE) has received the Dipl.-Ing. degree from the University of the Federal Armed Forces, Munich in 1979 and the Dr.-Ing. degree from Ruhr-University, Bochum in 1991. In 1987, he joined the Fraunhofer Institute for Applied Solid State Physics, Freiburg and worked on device modelling and circuit design. Since 1996, he is Professor at the University of Stuttgart. His main research interests are on design, modelling and characterization of electronic and optoelectronic devices and integrated circuits.